Citation: Mostefa Meddah, Salah Amroune, Mohamad Fnides, et al. Experimental investigation of the influence of tribological parameters on the fretting wear behaviour of tungsten carbide WC-Co: Effects of load, duration, and frequency. *Journal of Harbin Institute of Technology (New Series)*. DOI:10.11916/j.issn.1005-9113.2025074

Experimental Investigation of the Influence of Tribological Parameters on the Fretting Wear Behaviour of Tungsten Carbide WC-Co: Effects of Load, Duration, and Frequency

Mostefa Meddah[1], *Salah Amroune*[1,2*], *Mohamad Fnides*[3] *and Nadir Douib*[1]

(*1.Mechanical Department, Faculty of Technology, University of M'sila, M'sila 28000, Algeria;*
2.Materials and Structural Mechanics Laboratory (LMMS), University of M'sila, M'sila 28000, Algeria;
3.Higher School of Technological Education in Skikda, Skikda 21000, Algeria)

Abstract: A comprehensive experimental investigation was designed to explore the fretting wear behaviour of tungsten carbide WC-Co (25% cobalt), a cermet known for its exceptional wear and deformation resistance in harsh industrial settings. The study systematically examined the effects of three primary parameters—normal load (ranging from 1 to 4 N), contact duration (2 to 120 min), and vibration frequency (10.75 to 19.66 Hz)—using a custom-built ball-on-flat test rig operating under dry conditions. A multifactorial analysis of variance (ANOVA) was employed to assess the individual influence of each parameter on material mass loss. Findings reveal that both load and contact duration have a highly significant impact, whereas frequency shows a moderate but statistically meaningful effect. A nonlinear interaction between the parameters and the wear response was observed, characterised by an initial running-in phase transitioning into a steady-state wear regime. Microscopic analysis of the wear scars uncovered two distinct zones: a central, nearly circular adhesion zone and a peripheral elliptical sliding area. These morphological patterns were found to correlate closely with the measured mass loss. The results show that both load and contact duration have significant effects on mass loss (ANOVA, $p < 0.001$), and the developed regression models explain over 96% of the variance, providing quantitative prediction tools for wear.

Keywords: fretting wear, tungsten carbide, materials tribology, vibration-induced wear, tribological parameters, wear mechanisms, WC-Co, mechanical contact

CLC number: TH117.1 **Document code**: A **Article ID**: 1005-9113(2025)00-0000-15

0 Introduction

Fretting wear, often referred to as micro-motion wear, is a localized surface damage phenomenon that occurs at the contact interface between materials subjected to small-amplitude oscillatory displacements under load. This form of wear is particularly insidious because it develops in confined contact regions and under conditions that may not seem severe at first glance. Nonetheless, it can lead to serious material degradation, including crack initiation, debris formation, surface fatigue, and ultimately, failure of mechanical components[1-2]. Fretting is particularly prevalent in industrial systems that inherently experience cyclic loads or vibrations, such as aerospace structures, automotive assemblies, and biomedical implants [3-5]. In such applications, even minimal relative movement between contacting surfaces can initiate rapid damage accumulation, compromising reliability and performance.

The complexity of fretting wear lies in the intricate interactions between mechanical stress, material microstructure, environmental effects, and tribological parameters such as load, displacement amplitude, and frequency. While this wear mechanism has been extensively studied for certain classes of materials, there remains a significant gap in understanding how advanced engineering materials such as tungsten carbide-cobalt (WC-Co) behave

Received 2025-07-30.
Corresponding author: Salah Amroune, Ph.D, Professor. Email: salah.amroune@univ-msila.dz.

under fretting conditions. WC-Co is a cermet composed of hard tungsten carbide particles embedded within a ductile cobalt matrix, combining exceptional hardness and wear resistance with moderate toughness[6-7]. Its widespread use spans across cutting tools, dies, nozzles, and orthopaedic implants, where high-performance wear properties are critical[8-10].

Despite its extensive industrial relevance, the behaviour of WC-Co under fretting wear remains underexplored, particularly when multiple tribological parameters interact. Most available literature[11-12] has focused on conventional wear mechanisms such as abrasion, erosion, or adhesive wear under steady-state conditions, while overlooking the early, transient wear stages that often dominate in fretting situations[12-13]. These initial phases—commonly referred to as the running-in period—are characterised by unstable contact, rapid material removal, and evolving surface topography. Neglecting this stage can lead to an incomplete understanding of long-term wear performance and inaccurate life predictions[14-15].

Moreover, past studies[11,16] on WC-Co under fretting loading typically consider isolated parameters, such as normal load or frequency, without addressing the complex interplay between them. Yet, it is this interaction that often determines the dominant wear mechanisms—whether adhesive, abrasive, or oxidative—and the overall wear rate[17]. For instance, changes in contact frequency can influence heat generation and oxidation kinetics, while load and contact duration determine the extent of plastic deformation and microcrack propagation. Therefore, a multifactorial, statistically robust investigation is needed to accurately quantify the influence of these parameters and map the wear regimes governing WC-Co under realistic service conditions.

Recent contributions[18-19] have examined advanced fretting wear mechanisms and mathematical modelling in WC-Co and similar materials. These studies highlight the need for integrated approaches that combine in-depth experimentation and statistical analysis—an aspect our current work addresses. This study aims to address this gap by offering a comprehensive experimental investigation into the combined effects of applied load, contact duration, and vibration frequency on the fretting wear behaviour of WC-Co. Our methodological approach integrates systematic tribological testing with advanced microstructural characterisation to establish quantitative relationships between test parameters and damage mechanisms. The findings provide essential data for predictive wear modelling and offer practical perspectives for optimising the tribological performance of mechanical systems incorporating this material.

Our study makes a distinctive contribution by focusing on the often-overlooked transient wear phase and revealing nonlinear interactions among tribological parameters using robust regression modeling (ANOVA (analysis of variance) and RSM (response surface methodology)). Unlike prior literature[20-21], which mostly examines variable effects in isolation or under constant loading conditions, our results reveal how parameter interdependencies drive fretting damage. The predictive models developed allow estimation of mass loss based on selected input conditions, thereby providing practical tools for process optimization and foundation data for fatigue and life-prediction modeling. This integrative methodology not only fills a significant gap in fretting wear research but also offers transferable insights for optimizing the performance and longevity of WC-Co components in dynamic mechanical systems.

1 Materials and Methods

1.1 Materials Used

The test specimens were flat plates of WC-Co containing 25 wt% cobalt as a binder phase. Each plate measured 30 mm×10 mm×5 mm and exhibited a hardness of approximately 1600 HV, providing the high resistance to deformation characteristic of cemented carbides. The counter body consisted of steel balls (Z200), 9.5 mm in diameter and 700 HV in hardness. This material pairing was chosen to ensure a pronounced mechanical property contrast for effective investigation of fretting wear mechanisms.

1.2 Sample Preparation

All WC-Co plates were sequentially ground using SiC abrasive papers up to P1000 grit (average grain size≈18-20 μm), then polished with 1 μm diamond suspension on a felt pad to obtain a mirror-like finish. After polishing, the samples were ultrasonically cleaned in absolute ethanol for 15 min and dried at 60 ℃ for 2 h to ensure a consistent, contaminant-free surface. Steel balls were cleaned in absolute ethanol before each test to remove any residual surface impurities.

Surface roughness (R_a) was evaluated for both

materials using a MITUTOYO Surftest-4 profilometer. The WC-Co samples exhibited an average R_a of 0.12± 0.02 μm, consistent with typical results obtained by polishing with P1000 grit followed by 1 μm diamond paste. The steel balls had an R_a of 0.035±0.005 μm, ensuring a stable, smooth initial contact surface.

All specimens were inspected using optical microscopy to confirm the absence of visible surface defects before testing.

A rigorous surface preparation protocol was implemented to ensure repeatable test results. Initially, a pre-lapping stage was performed using a dual-disc rotary machine (maximum 300 r/min), with water lubrication to prevent overheating. This was followed by final polishing with 1 μm diamond paste on a felt pad soaked in solvent. The samples were then ultrasonically cleaned in absolute ethanol for 15 min and dried in an oven at 60 ℃ for 2 h.

1.3 Experimental Setup

The fretting wear tests were performed using a custom-designed apparatus (as shown in Fig. 1) specifically developed to enable precise control of tribological parameters and to replicate reciprocating contact conditions. It was equipped with a variable-speed electric motor (70 V－75 V) powered by a transformer, and a transmission mechanism that converted rotary motion to linear motion via a connecting rod and sample bearing. A load cell with a force sensor (measurement range: 0−5 N; resolution: 0.01 N) enabled accurate force monitoring. The actual vibration frequency was measured using a digital tachometer. The samples were securely fixed using a self-clamping vice with an anti-vibration system to ensure stability and precision throughout the tests.

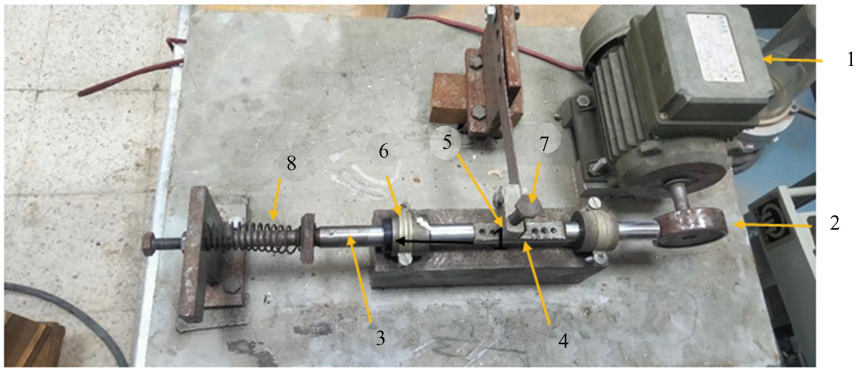

1—Electric motor; 2—Eccentric disk; 3—Sample holder rod; 4—Vice; 5—Fixed steel ball; 6—Guide and bearing; 7—Load cell; 8—Return spring

Fig.1 Fretting wear testing apparatus

The tribo-system consists of eight main elements. The electric motor, mounted on a frame and powered by a transformer, drives an eccentric disk. The disk's axis is intentionally offset relative to the motor shaft axis. As the disk rotates, it comes into contact with one side of the sample holder rod, pushing it forward by direct contact (with no rigid attachment). When the disk rotates past the contact point, the return spring at the opposite end of the rod returns it, ensuring consistent reciprocating (back-and-forth) motion.

This reciprocating motion is thus transferred to the WC-Co sample, which is mounted in a vice fixed onto the moving rod and slides linearly beneath the fixed steel ball. Guides and bearings ensure precise alignment and smooth translation of the rod. The displacement amplitude is determined by the offset between the motor shaft axis and the disk axis. The normal force is applied and precisely measured with the load cell, and the actual vibration frequency is monitored and adjusted using a digital tachometer.

The friction (wear) path in our experiments consisted of a linear reciprocating motion with an estimated stroke length of approximately 0.1 mm (100 μm), maintained parallel to the specimen's surface. This configuration was chosen to ensure controlled and repeatable tribological conditions, enabling a balance between localized contact mechanics and sufficient wear measurement sensitivity. Such a stroke amplitude (~0.1 mm) is widely recognized and routinely employed in microscale fretting wear studies, similar wear behaviors have been observed, particularly in ball-on-flat reciprocating setups operating at frequencies and loads comparable to those employed in our experiments, as reported by Kontou et al.[22] and

Kolbas et al.[23].

1.4 Experimental Protocol

The experimental plan was designed to examine the influence of three independent variables: normal load (1, 2, 3, and 4 N), test duration (2, 5, 10, 15, 20, 30, 60, and 120 min), and vibration frequency (based on applied voltage; as shown in Table 1). For each parameter combination, a strict procedure was followed: initial mass measurement using an analytical balance (accuracy ±0.0001 g), careful alignment and mounting of sample and ball, test execution under controlled environmental conditions (ambient temperature 22 ± 1 ℃, relative humidity 45 ± 5%), final mass measurement after ultrasonic cleaning, and morphological characterisation of wear scars using a metallurgical microscope.

The total number of fretting cycles in each test was calculated by multiplying the vibration frequency (Hz) by the test duration (in seconds). Depending on the chosen parameters, this yielded a range from approximately 1290 cycles (e.g., 10.75 Hz, 2 min) up to 141552 cycles (e.g., 19.66 Hz, 120 min). This methodology aligns with prior tribological studies using ball-on-disc analysis on carbide materials: Dembiczak et al.[24] investigated abrasion wear of commercial cutting inserts under dry fretting conditions using a ZrO_2 ball at 55 N; similarly, Náprstková et al.[25] employed a ball-on-disc setup to assess abrasive behavior in carbide drawing dies.

Table 1 Standardized test matrix

Voltage(V)	Load(N)	Frequency(Hz)	Duration(min)
70	1	11.66	2, 5, 10, 15, 20, 30, 60, 120
	2	11.50	2, 5, 10, 15, 20, 30, 60, 120
	3	11.25	2, 5, 10, 15, 20, 30, 60, 120
	4	10.75	2, 5, 10, 15, 20, 30, 60, 120
75	2	19.66	2, 5, 10, 15, 20, 30, 60, 120
	3	19.50	2, 5, 10, 15, 20, 30, 60, 120

2 Results and Discussion

2.1 Wear Regimes: Running-In and Stabilisation

The examination of mass loss (Δm) trends, as depicted in Figs. 2 and 3, highlights a clear two-stage wear progression during the fretting tests. The first phase, commonly referred to as the running-in period, lasts for the first 30 min of contact. This stage is marked by a sharp and rapid increase in mass loss, indicating intense surface interactions and accelerated material removal. Such behaviour is typical in tribological systems, where fresh contact surfaces undergo mechanical and microstructural adjustments due to frictional forces, localized stress concentrations, and asperity breakdown. During this phase, wear mechanisms such as micro-ploughing, adhesion, and localized plastic deformation dominate, contributing to the rapid degradation observed. Following this initial period, the system transitions into a second, more stable wear regime. In this steady-state phase, the rate of mass loss significantly decreases and becomes more uniform over time, suggesting that the contact surfaces have reached a quasi-equilibrium condition. Surface conformity improves, and the wear mechanisms shift towards more predictable forms such as mild oxidative or abrasive wear. This dual-phase wear pattern is consistent with the findings reported by Khonsari et al.[14], who highlighted the importance of the running-in phase as a determinant of the long-term evolution and stability of tribological interfaces. According to their analysis, the early stage of wear plays a crucial role in shaping the morphology of the contact zone and influencing the subsequent wear performance. Therefore, understanding and controlling the parameters governing the running-in period is essential to enhancing the durability and efficiency of mechanical systems operating under fretting conditions.

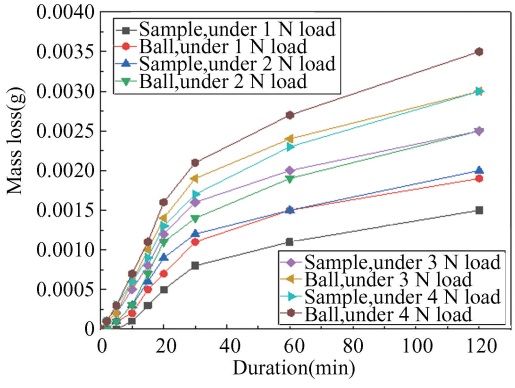

Fig.2 Evolution of mass loss Δm as a function of time for different normal loads at 70 V

2.2 Effect of Load

Experimental results demonstrate that the applied normal load significantly influences the progression of fretting wear. Increasing the load from 1 to 4 N results in a pronounced increase in mass loss, particularly during the initial running-in phase (less than 30 min). It was observed that the wear resistance of the sample exceeded that of the steel ball. This behaviour can be attributed to increased contact pressure and mechanical

energy injected into the system, which accelerate interface degradation[14].

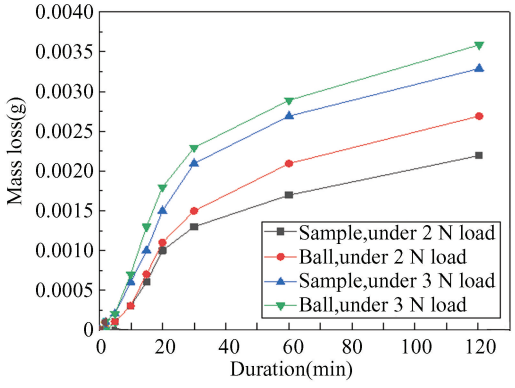

Fig.3 Evolution of mass loss Δm as a function of time for different normal loads at 75 V

Wear scars indicate a progressive widening of the contact area with increasing load, reflecting a transition from point contact to more extended contact. This evolution is consistent with Hertzian theory[26], which predicts that the contact area enlarges with applied normal force. Microscopic analysis reveals intensified adhesion and material detachment at higher loads, suggesting a shift towards a more adhesive wear mechanism.

Previous studies confirm this trend: Thirumalvalavan et al.[8] showed that higher loads in similar systems result in more aggressive wear of thermally sprayed WC-Co coatings. This behaviour is attributed to increased interfacial shear stress that promotes microcrack initiation and propagation under cyclic loading.

These findings reinforce the understanding that normal load is not only a key factor affecting wear rate but also influences the dominant wear mechanisms (abrasion, adhesion, and cracking). Thus, controlling this parameter is essential for optimising the tribological performance of WC-Co/steel interfaces in vibration-prone applications.

2.3 Effect of Frequency

Figs.4 and 5 present data for two frequency levels (11.5 and 19.66 Hz). The results indicate a greater mass loss at higher frequency, particularly during the running-in phase. This increase can be explained by the higher number of sliding cycles per unit time, which amplifies interfacial shear and thus the rate of material removal. These findings are consistent with the results of Shi et al.[27] who reported that higher frequencies induce more pronounced sliding and increase adhesive wear in aluminium bronze coatings.

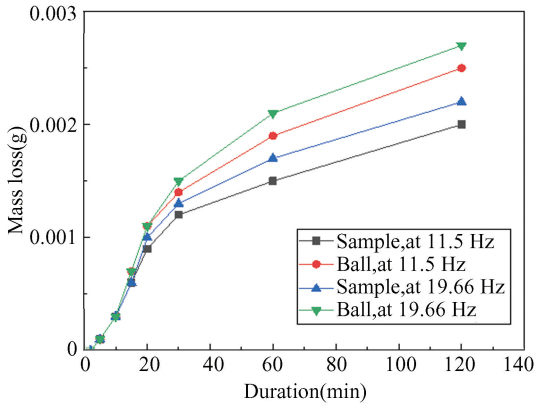

Fig.4 Evolution of mass loss Δm as a function of time for a 2 N load at 11.5 and 19.66 Hz

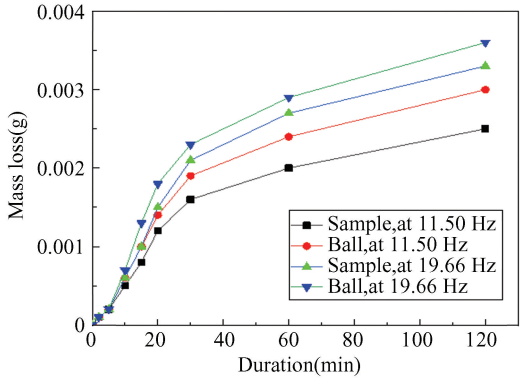

Fig.5 Evolution of mass loss Δm as a function of time for a 3 N load at 11.5 and 19.66 Hz

2.4 Wear Scar Dimensions

The size of the wear scar was measured using a NEOPHOT optical microscope. Figs. 6 and 7 show that scar dimensions increase over time. During the first 30 min, both the adhesion zone and the contact area expand rapidly. Beyond this duration, however, the adhesion zone tends to stabilise, while the contact area continues to evolve more slowly.

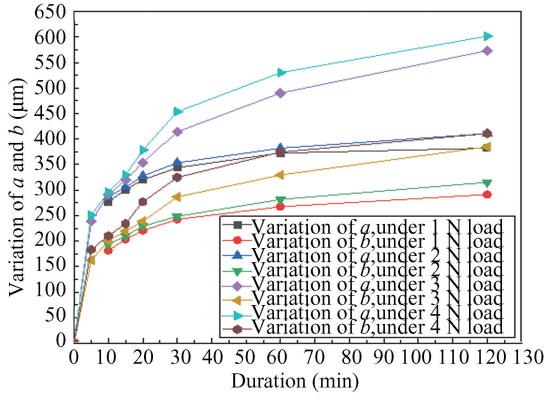

Fig.6 Size of the imprint as a function of time(a) and applied loads(b), at 70 V

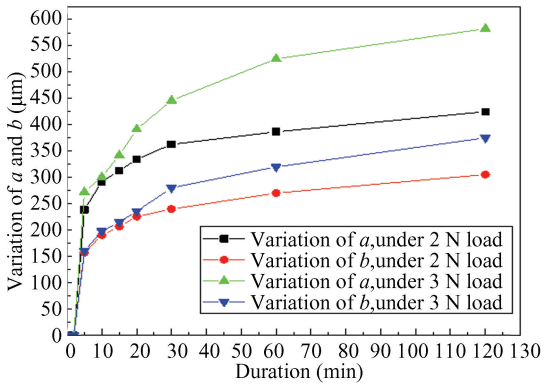

Fig.7 Size of the imprint as a function of time(*a*) and applied loads(*b*), at 75 V

2.5 Influence of Load on Adhesion and Contact Zones

Fig. 8 demonstrates that both the adhesion and the contact zone increase in size with higher applied loads. This highlights the strong dependence of contact mechanics on the load, as increased force enlarges the real contact area and intensifies interfacial stresses.

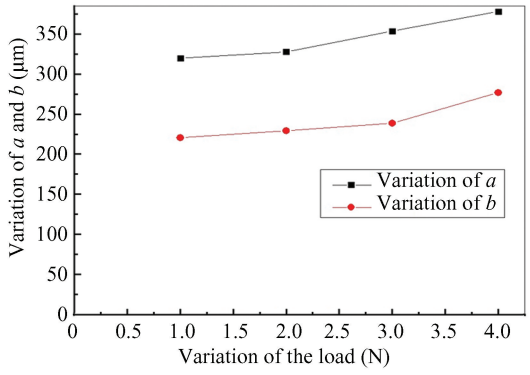

Fig.8 Variation of *a* and *b* with normal force, for 20 min

2.6 Microscopic Observations

Figs. 9 to 12 show that morphological analysis of the wear scars reveals two distinct regions: a central adhesion zone, indicating strong interfacial bonding, and a peripheral sliding zone associated with abrasive wear. This morphology, although no tribofilm was applied, agrees with the findings by Fischer et al.[28], who described localised material detachment and micro-grooving at the contact edges. The quasi-circular central zone corresponds to intense adhesion between surfaces, while the elliptical periphery reflects relative motion marked by parallel striations characteristic of abrasive mechanisms.

The evolution of scar dimensions (axes *a* and *b*) during the initial period, especially under high loads, defines the wearing-in phase, characterised by rapid wear due to non-uniform stress distribution. After about 30 min, a geometric adaptation of the contact occurs, leading to more uniform mechanical loading and surface saturation[29].

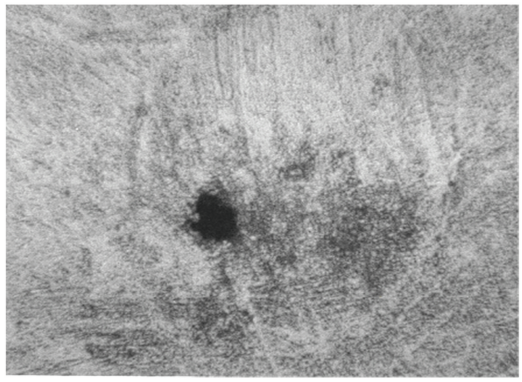

Fig.9 Image of the imprint under 3 N load, after 120 min at 11.5 Hz, magnified 960 times

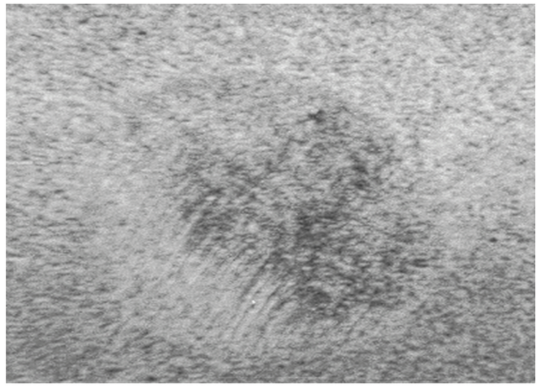

Fig.10 Image of the imprint under 3 N load, after 60 min at 11.5 Hz, magnified 960 times

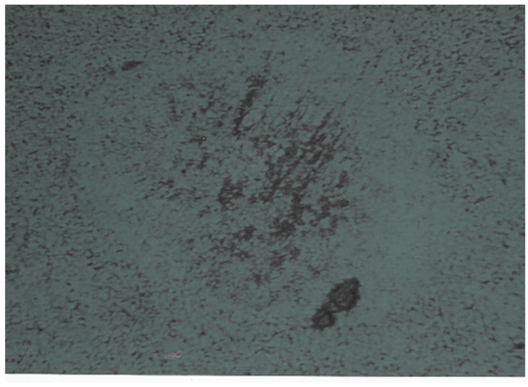

Fig.11 Image of the imprint under 2 N load, at 11.5 Hz, after 120 min, magnified 960 times

The wear behaviour in this ball-on-flat configuration differs significantly from traditional flat-

on-flat systems. At short durations, the contact is point-like, generating high localised pressure. As time progresses (beyond 30 min), the contact area broadens, reducing local pressure, and changes in dimensions (a and b) become less rapid. The mass loss curves from Figs. 9 to 12 show two regimes: initially, a sharp mass loss due to concentrated pressure and point contact (running-in), followed by stabilised wear as the contact area increases and pressure decreases.

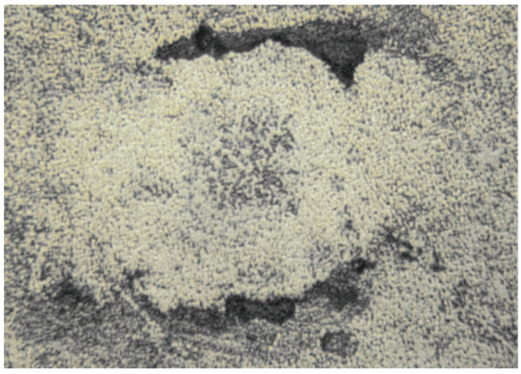

Fig.12 Image of the imprint under 4 N load, at 11.5 Hz, after 60 min, magnified 960 times

Regarding the influence of frequency, limitations in the test device—specifically its restriction to two voltages (70 V and 75 V)—prevent comprehensive analysis. However, results suggest that higher frequency tends to increase mass loss due to more intense vibrational input.

Microscopic analysis revealed that these morphological patterns strongly correlate with the measured mass loss. In particular, specimens with larger adhesion zones and elongated sliding areas consistently exhibited higher wear. This qualitative trend was supported by ANOVA results, which showed that both load and contact duration significantly affect mass loss ($p<0.001$). Moreover, the regression models developed in Section 2.7 accounted for over 96% of the variance in wear, reinforcing the relevance of the visual observations as indicators of wear progression. It should be noted that quantitative characterization in this study was limited to measurements of the major and minor axes of the elliptical wear scars using optical microscopy. Due to equipment limitations, no depth profiling, crack density evaluation, or SEM imaging could be performed. While the observed morphology—with a central adhesion zone and a peripheral sliding area—reflects established adhesive and abrasive wear mechanisms, a deeper understanding of subsurface and microstructural damage would require advanced methods such as profilometry or scanning electron microscopy. These limitations are acknowledged, and future studies are encouraged to employ expanded surface and subsurface analyses for a more comprehensive interpretation.

2.7 RSM

RSM is a suite of mathematical and statistical techniques for modelling and analysing systems in which a target response depends on multiple input variables[20-21,30-36]. Its primary aim is to optimise that response. In this study, a quadratic model was developed based on 72 experimental trials. The model was constructed using dedicated design software employing an RSM-based approach. Three factors—voltage (A), load (B), and time (C)—were analysed using an optimal design methodology. Response surfaces were generated to compare RSM model predictions with experimental data. The characteristics and levels of the studied factors are summarised in Table 2.

Table 2 Factors and levels used in the experimental plan

Levels	A(V)	B(N)	C(min)
1	70	1	2
2	75	2	5
3	–	3	10
4	–	4	15
5	–	–	20
6	–	–	30
7	–	–	60
8	–	–	120

2.8 Quadratic Modelling of the Responses: SML and BML

The most suitable quadratic models for the two responses—Sample Mass Loss (SML) and Ball Mass Loss (BML)—were developed as regression equations using coded variables (Eqs. (1) and (2)). Expressing the models in coded form allows for straightforward interpretation of each factor's effect. In this representation, a coefficient of +1 corresponds to a high level of the factor, and −1 to a low level. By examining the coefficients, it is possible to rank the impact of each factor on the measured responses and assess potential interactions.

$$SML = 0.00215812 + 0.000149817 \times A + 0.000586436 \times B + 0.00122831 \times C + 4.61667 \times 10^{-5} \times AB + 0.000126443 \times AC + 0.000401962 \times BC + 0 \times A^2 - 7.1875 \times 10^{-5} \times B^2 - 0.000892416 \times C^2 \quad (1)$$

$$BML = 0.00256718 + 0.000151784 \times A + 0.000607767 \times B + 0.00145969 \times C + 4.55 \times 10^{-5} \times AB + 0.000121632 \times AC + 0.000415555 \times BC + 0 \times A^2 - 5.625 \times 10^{-6} \times B^2 - 0.00110647 \times C^2 \quad (2)$$

2.9 Analysis and Discussion of Figures-Model Validation

Fig.13 presents the statistical diagnostics applied to the regression models developed for the two experimental responses: SML and BML. These diagnostics include plots of predicted versus observed values (Figs. 13 (a) and (c)) as well as normal probability plots of residuals (Figs.13 (b) and (d)).

The goodness-of-fit for the regression model for SML is illustrated in Fig. 13 (a), which shows the correlation between predicted and observed values. The scatter plot follows an upward linear distribution along the identity line, indicating strong agreement between experimental data and model predictions. The SML response values range from 0 to 0.0036 g, as shown by the colour scale on the left of the graph. Most data points, coloured light blue, green, and yellow and corresponding to values between 0.0010 and 0.0030 g, align well along the diagonal, with a maximum deviation of approximately ±0.0005 g. This distribution indicates that the model accurately predicts the overall trend, despite slight deviations at the higher end of the data range.

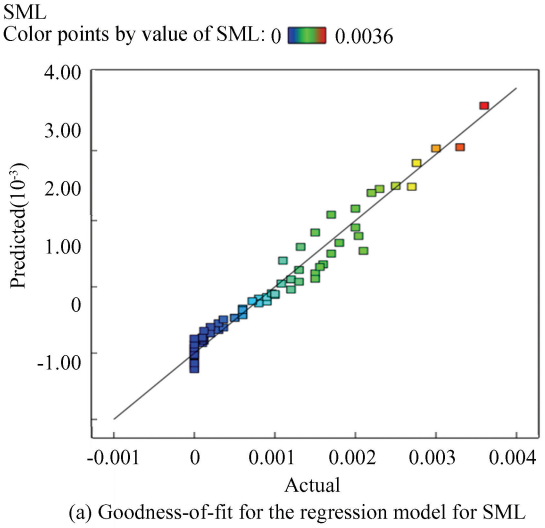

(a) Goodness-of-fit for the regression model for SML

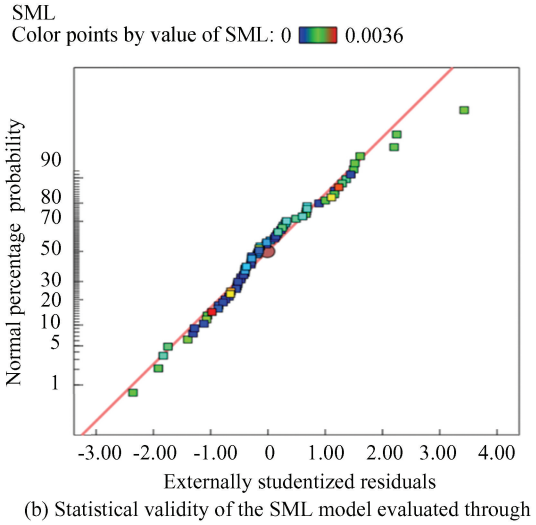

(b) Statistical validity of the SML model evaluated through residual analysis

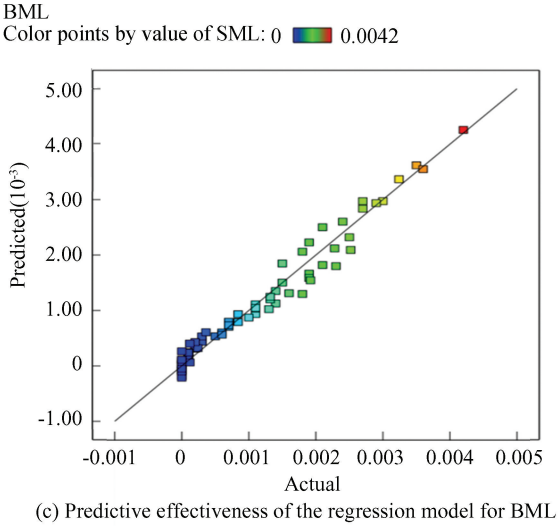

(c) Predictive effectiveness of the regression model for BML

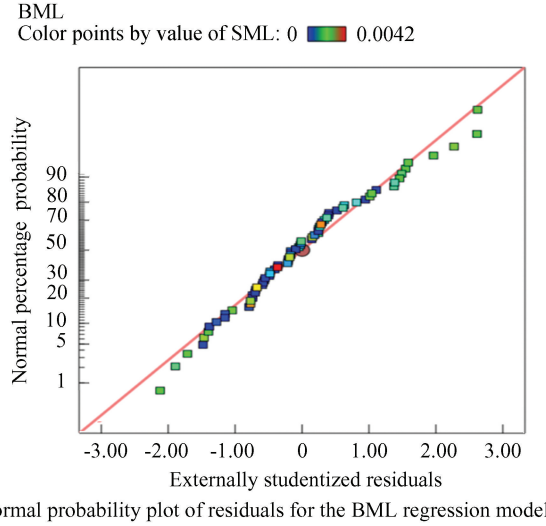

(d) Normal probability plot of residuals for the BML regression model

Fig.13 Normal probability of residuals for SML and BML

The statistical validity of the SML model is further evaluated through residual analysis shown in Fig. 13(b), which displays the normal probability plot of residuals. The distribution of points follows a near-linear pattern, suggesting approximate normality. However, a few data points at the extremes, particularly those beyond ±2.5, deviate slightly from the reference line, potentially indicating the presence of influential values or minor heteroscedasticity. The residuals range from approximately −2.9 to +3.4, with around 95% of the data falling within −2 to +2, which remains acceptable for a normally distributed residual set. These results suggest that the model is generally well-fitted, though a refinement could improve its predictive accuracy at the tails of the distribution.

The predictive effectiveness of the regression model for BML is illustrated in Fig. 13(c), which shows the predicted versus observed values. This graph reveals even tighter alignment than observed in the SML model, with colour-coded points ranging from dark blue to red that closely align along the identity line. The BML response ranges from 0 to 0.0042 g, and the maximum deviation between experimental and predicted values remains below ±0.0004 g. The dense clustering of points in the interval [0.0015, 0.0035] g confirms the high precision of the model in this region and its ability to reliably represent the global trend of the phenomenon.

Fig. 13(d) displays the normal probability plot of residuals for the BML regression model. The residuals are nearly perfectly aligned along the theoretical line, indicating a well-maintained normal distribution. Residuals range from −2.8 to +3.1, with a high concentration between −1.5 and +1.5. No outliers or significant deviations are observed, confirming the model's stability. This consistent residual distribution confirms the statistical validity of the BML model and supports appear more precise than those of the SML model.

The analysis of these four figures confirms that both regression models exhibit solid statistical validity, with overall satisfactory agreement between observed and predicted values. Nevertheless, the BML model demonstrates superior performance in terms of both linearity and residual normality. This may be attributed to the BML variable's higher sensitivity to the studied factors or to reduced experimental variability.

2.10 Response Surfaces for SML and BML

In this study, two response surfaces were generated to analyse the evolution of SML and BML as a function of *A* and *B*, with a test time of 60 min fixed.

Fig. 14(a), which illustrates the response surface for SML, reveals a clear and nearly linear increase in mass loss as both voltage and load increase. Although the surface displays slight convexity, the linear contribution remains dominant, suggesting that the quadratic and interaction effects are minimal within the investigated range.

Similarly, Fig. 14(b), showing the response surface for BML, confirms the same trend. The BML increases steadily with both rising voltage and load, highlighting a similar quasi-linear behaviour.

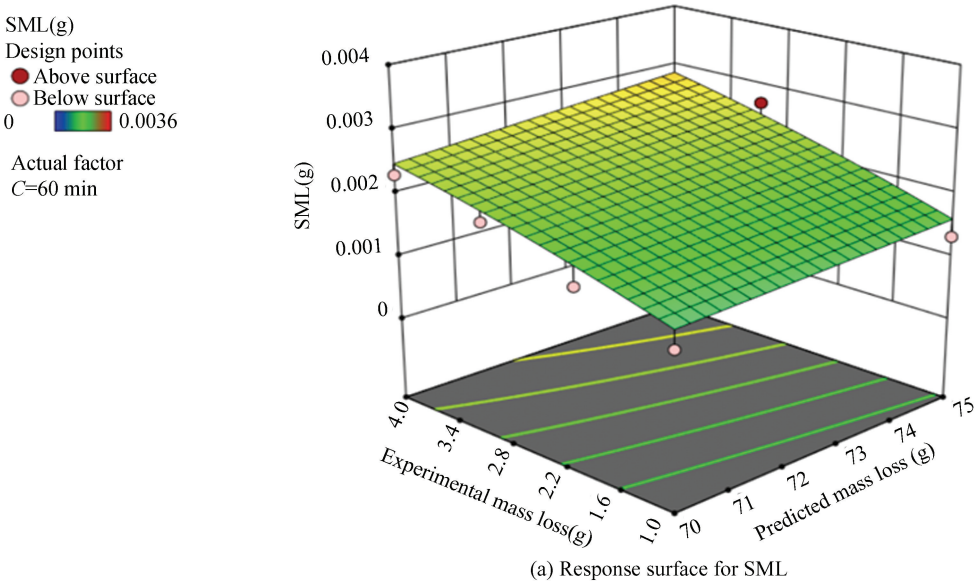

(a) Response surface for SML

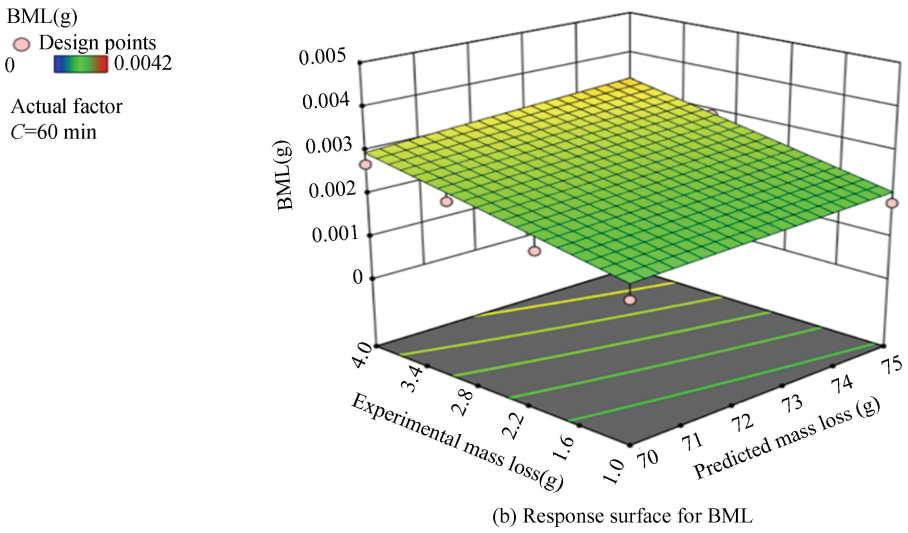

(b) Response surface for BML

Fig.14 Response surface for delamination, SML and BML

The influence of voltage (*A*) is particularly pronounced. At constant load, increasing the voltage from 70 to 75 V results in a rise in SML from approximately 0.001 to over 0.003 g, and in BML from around 0.0015 to nearly 0.004 g. This underlines the strong sensitivity of both responses to electrical input, with BML showing slightly greater responsiveness.

The effect of load (*B*) is also significant. At fixed voltage, raising the load from 1 to 4 N causes SML to grow from approximately 0.001 to 0.003 g, while BML increases from 0.002 to about 0.0035 g. These results demonstrate the cumulative and almost linear influence of mechanical load, reinforcing its role in the wear process.

At the extreme upper-right corner of both surfaces—corresponding to the highest voltage (75 V) and load (4 N)—the maximum values are recorded, with SML reaching around 0.0036 g and BML about 0.0042 g. Conversely, the minimum values occur at the lower-left corner (70 V, 1 N).

The close proximity of the experimental data points (dots) to the surfaces in both figures confirms the high predictive accuracy of the quadratic models.

In conclusion, Figs. 14 (a) and 14 (b) demonstrate that simultaneous increases in voltage and load cause a near-linear rise in both SML and BML. The RSM-based quadratic models provide reliable insight into these trends and serve as effective tools for optimising the wear conditions by fine-tuning operational parameters within the studied range.

2.11 ANOVA for the Quadratic Model

ANOVA applied to the quadratic models developed for SML and BML serves as a fundamental statistical tool to evaluate the influence of experimental factors and their interactions. It helps determine whether observed variations in the responses are statistically significant or merely due to random noise.

This analysis identifies both the main factors and interaction effects that significantly impact the two studied responses. By highlighting the most influential parameters, ANOVA enhances understanding of wear mechanisms and guides the optimisation of experimental conditions—ultimately improving tribological performance and material surface quality.

2.11.1 ANOVA analysis of the quadratic model-response: SML

ANOVA applied to the quadratic model developed for the SML response was used to assess the statistical relevance of the experimental factors: *A*, *B*, *C*, along with their interaction and quadratic effects. The results are presented in Table 3. The results indicate that the overall model is highly significant, with an *F*-value of 221.05 and a *p*-value lower than 0.0001. This suggests that the likelihood of the observed fit being due to random variation is nearly zero (<0.01%), fully justifying the use of this model for interpreting and predicting mass loss under different experimental conditions.

Table 3 ANOVA for quadratic model response 2: SML

Source	Sum of squares	Degree of freedom	Mean square	F-Value	p-Value	Contribution (%)	Remark
Model	1.000×10^{-4}	8	7.314×10^{-6}	221.05	< 0.0001	96.56	Significant
A	9.429×10^{-7}	1	9.429×10^{-7}	28.50	<0.0001	1.55	Significant
B	8.026×10^{-6}	1	8.026×10^{-6}	242.56	< 0.0001	13.23	Significant
C	4.032×10^{-5}	1	4.032×10^{-5}	1210.69	<0.0001	66.47	Significant
AB	8.525×10^{-8}	1	8.525×10^{-8}	2.58	0.1135	0.14	Insignificant
AC	4.273×10^{-7}	1	4.273×10^{-7}	12.91	0.0006	0.70	Insignificant
BC	2.399×10^{-6}	1	2.399×10^{-6}	72.51	<0.0001	3.96	Significant
A^2	0	0	–	–	–	Negligible	Insignificant
B^2	7.347×10^{-8}	1	7.347×10^{-8}	2.22	0.1412	0.12	Insignificant
C^2	6.297×10^{-6}	1	6.297×10^{-6}	190.30	<0.0001	10.38	Significant
Residual	2.085×10^{-6}	63	3.309×10^{-8}	–	–	–	–
Corrected total	1.000×10^{-4}	71	–	–	–	–	–

Regarding the main effects, all three studied factors are highly significant. Factor A shows an F-value of 28.50 with a mean square of 9.429×10^{-7}, reflecting a measurable but relatively moderate influence on mass loss. Factor B has a much stronger impact, with an F-value of 242.56 and a mean square of 8.026×10^{-6}, indicating that increasing the load considerably intensifies sample wear. Factor C stands out as the most influential parameter, with an exceptionally high F-value of 1210.69 and a mean square of approximately 4.032×10^{-5}, confirming that exposure duration is the dominant factor driving mass loss.

Concerning interaction effects, the AB interaction (voltage×load) is not significant ($F = 2.58$; $p = 0.1135$), suggesting a negligible combined effect. In contrast, the AC interaction (voltage × time) is significant ($F = 12.91$; $p = 0.0006$), indicating a moderate synergistic effect between applied voltage and exposure duration. The BC interaction (load × time) is particularly influential, with an F-value of 72.51 and a p-value<0.0001, demonstrating that the combined effect of load and wear duration greatly amplifies material loss.

As for the quadratic terms, A^2 was not evaluated (zero degrees of freedom), likely due to either an absence of effect or prior elimination during model selection. The B^2 term is not significant ($F=2.22$; $p=0.1412$), indicating a primarily linear relationship between load and mass loss. Conversely, C^2 is highly significant ($F = 190.30$; $p<0.0001$), confirming a nonlinear response to time and consistent with an increasing quadratic effect as exposure duration lengthens.

Finally, the residual error is low, with a sum of squares of 2.085×10^{-6}, 63 degrees of freedom, and a mean square of 3.309×10^{-6}, confirming the model's excellent fit to the experimental data.

In conclusion, the ANOVA shows that wear time (C) is by far the dominant factor influencing SML, followed by load (B), while voltage (A), though statistically significant, exerts a comparatively smaller effect. The BC interaction and the C^2 quadratic term reinforce the model's robustness, whereas the AB and B^2 terms, being non-significant, could be excluded from a simplified version of the model. These findings provide a solid analytical framework for optimising test conditions and improving understanding of the underlying wear mechanisms.

These results confirm that C is the dominant factor influencing the SML response, exerting the strongest effect among all variables. It is followed by B and the quadratic term C^2, which also contribute noticeably, though to a lesser extent. In contrast, the remaining interaction and quadratic effects have only a marginal impact, highlighting their limited significance in the studied experimental range.

The model F-value of 221.05 indicates that the regression model is highly significant. There is only a 0.01% probability that such a high F-value could result from random noise, confirming the statistical robustness of the model.

p-values less than 0.0500 suggest that the corresponding model terms are statistically significant.

In this case, the terms A, B, C, AC, BC, and C^2 have a significant effect on the response. Conversely, terms with p-values greater than 0.1000 are considered not significant. When a model includes several non-significant terms (excluding those necessary for maintaining model hierarchy), applying model reduction techniques can enhance model simplicity and predictive accuracy.

The predictive determination coefficient (R^2-pred) of 0.9520 is in good agreement with the adjusted R^2 of 0.9612, with a difference below 0.2, which reflects the model's consistency and robustness.

Moreover, the adequate precision value, which evaluates the signal-to-noise ratio, is 61.804. This value, far exceeding the recommended threshold of 4, indicates a sufficiently strong signal for the model to be considered reliable. These values are summarised in Table 4.

Therefore, the model can be regarded as both relevant and effective for guiding exploration and optimisation within the studied experimental space.

2.11.2 ANOVA analysis of the quadratic model-response: BML

The ANOVA applied to the quadratic model for BML confirms the statistical robustness of the fit: the overall F-value of 235.61, with a p-value < 0.0001, indicates less than a 0.01% probability that the model's accuracy is due to chance. The detailed ANOVA results are presented in Table 5. All three main effects are significant: A has a noticeable but moderate influence ($F = 22.71$; $p < 0.0001$), B exerts a highly pronounced effect ($F = 202.29$; $p < 0.0001$), while C overwhelmingly dominates the response behaviour ($F = 1327.59$; $p < 0.0001$).

Table 4 Model performance metrics for the SML quadratic regression

Standard deviation	Mean	Coefficient of variation (%)	R^2	Adjusted R^2	Predicted R^2	Adequate precision
0.0002	0.0009	19.81	0.9656	0.9612	0.9520	61.8038

Table 5 ANOVA for quadratic model response 2: BML

Source	Sum of squares	Degree of freedom	Mean square	F-Value	p-Value	Contribution (%)	Remark
Model	1.000×10^{-4}	8	0	235.6100	<0.0001	96.77	Significant
A	9.678×10^{-7}	1	9.678×10^{-7}	22.7100	<0.0001	0.77	Significant
B	8.620×10^{-6}	1	8.620×10^{-6}	202.2900	<0.0001	6.90	Significant
C	1.000×10^{-4}	1	1.000×10^{-4}	1327.5900	<0.0001	80.00	Significant
AB	8.281×10^{-8}	1	8.281×10^{-8}	1.9400	0.1682	0.07	Insignificant
AC	3.954×10^{-7}	1	3.954×10^{-7}	9.2800	0.0034	0.32	Insignificant
BC	2.564×10^{-6}	1	2.564×10^{-6}	60.1700	< 0.0001	2.05	Significant
A^2	0	0	–	–	–	Negligible	Insignificant
B^2	4.500×10^{-10}	1	4.500×10^{-10}	0.0106	0.9185	Negligible	Insignificant
C^2	9.679×10^{-6}	1	9.679×10^{-6}	227.1500	< 0.0001	7.74	Significant
Residual	2.685×10^{-6}	63	4.261×10^{-8}	–	–	–	–
Corrected total	1.000×10^{-4}	71	–	–	–	–	–

Among the interaction terms, the AC interaction (voltage×time) is significant ($F = 9.28$; $p = 0.0034$), as is the BC interaction (load × time), which is particularly important ($F = 60.17$; $p < 0.0001$). In contrast, the AB interaction is not significant ($F = 1.94$; $p = 0.1682$).

With respect to quadratic terms, C^2 is crucial ($F = 227.15$; $p < 0.0001$), indicating a nonlinear effect of time. Meanwhile, B^2 ($F = 0.0106$; $p = 0.9185$) contributes nothing meaningful, and A^2 is negligible. The residual error remains low (Sum of squares = 2.685×10^{-6}; MS = 4.261×10^{-8} over 63 degrees of freedom), confirming the model's strong fit to the experimental data.

In summary, wear time is clearly the dominant factor, followed by load, while voltage plays a secondary but non-negligible role. The load × time interaction and the quadratic term for time substantially reinforce the model, whereas terms such as AB and B^2 could be eliminated without impairing predictive

performance.

C is by far the most influential factor in the response (BML), contributing approximately 80% of the total variation. The C^2 and B terms also show notable contributions. Other terms exert marginal influence, with some, such as B^2 and AB, being nearly negligible, which justifies a potential simplification of the model without a significant loss of accuracy.

The predictive determination coefficient (R^2_pred = 0.9571) is in good agreement with the adjusted determination coefficient (R^2_adj = 0.9636), with a difference below 0.2. This close correspondence confirms the coherence between the model's explanatory power and its predictive capability. These statistical indicators are summarised in Table 6.

Table 6 Model performance metrics for the SML quadratic regression

Standard deviation	Mean	Coefficient of variation (%)	R^2	Adjusted R^2	Predicted R^2	Adequate precision
0.0002	0.0011	18.62	0.9677	0.9636	0.9571	61.2532

Furthermore, the adequate precision statistic, which evaluates the signal-to-noise ratio, shows a value of 61.235, well above the minimum recommended threshold of 4. This indicates that the model possesses a sufficiently strong signal to be reliably used for exploring the experimental space and navigating within the design domain.

3 Conclusions

This experimental study provides a deeper understanding of the tribological behaviour of tungsten carbide WC-Co (25% Co) under fretting wear conditions. The analysis specifically focused on the influence of three key parameters: normal load, contact duration, and vibration frequency.

Using a custom-designed experimental apparatus combined with a rigorous sample preparation and observation methodology, the main wear mechanisms at the microscopic scale were successfully identified.

The results showed that a transient running-in regime consistently precedes a stabilised wear phase. The transition between these two regimes is strongly influenced by the temporal evolution of contact conditions. The wear scars left by the ball exhibited a characteristic morphology, with a quasi-circular central adhesion zone and an elliptical peripheral sliding zone. The size of this scar increased with both load and time, before tending toward stabilisation, reflecting the progressive saturation of the contact area.

Furthermore, mass loss measurements revealed a gradual reduction in wear over time, linked to the increasing contact surface and the corresponding decrease in specific pressure. The effect of frequency was also confirmed, although only two voltage levels were explored due to equipment limitations. A higher vibration frequency tends to increase material loss, owing to more intense vibrational loading.

To interpret the experimental outcomes quantitatively and assess parameter interactions, statistical modeling techniques including ANOVA and RSM were employed. These tools enabled the development of predictive equations for wear loss, with strong correlation coefficients ($R^2 > 0.96$), offering practical insights for parameter optimization.

While the results presented here offer quantitative insight into the effects of tribological parameters on WC-Co under controlled laboratory conditions, these findings should not be interpreted as direct evidence for industrial performance improvement. Additional work is necessary to validate these results under real-world service conditions, compare alternative materials or coatings, and include life-cycle analysis before confirming practical performance gains. The models developed in this study serve as a foundation for further scientific investigation and optimization, not as definitive industrial solutions.

Ultimately, this study highlights the critical importance of controlling contact conditions in fretting wear phenomena and provides a solid foundation for optimising materials and tribological configurations in vibrational environments. The findings also open promising avenues for predictive modelling to improve the durability of mechanical components subjected to such stress conditions.

References

[1] Al-Rybaye H F H. Analysis of wear resistance aviation materials with titanium alloys. Kyiv: National Aviation University, 2021.

[2] Diomidis N. 9-Wear phenomena of metal joints. Wear of orthopaedic implants and artificial joints, Woodhead Publishing Series In Biomaterials, 2013: 246-277. DOI: 10.1533/9780857096128.1.246.

[3] Antunes R A, De Oliveira M C L. Corrosion fatigue of biomedical metallic alloys: mechanisms and mitigation. Acta Biomaterialia, 2012,8(3):937-962. DOI:10.1016/j.actbio.2011.09.012.

[4] Basu B, Kalin M. Tribology of Ceramics and Composites: A Materials Science Perspective. Hoboken: John Wiley & Sons, 2011.

[5] Moghadasi K, Isa M S M, Ariffin M A, et al. A review on biomedical implant materials and the effect of friction stir based techniques on their mechanical and tribological properties. Journal of Materials Research and Technology, 2022,17:1054-1121.DOI:10.1016/J.JMRT.2022.01.050.

[6] Enever A A. Performance evaluation of WC-12wt% Co as grinding wheel abrasive material by machining a titanium alloy.Stellenbosch: Stellenbosch University, 2016.

[7] Genga R M. Microstructure and properties of selected WC-cemented carbides manufactured by SPS method. Johannesburg: University of The Witwatersrand, 2014.

[8] Thirumalvalavan S, Perumal G, Senthilkumar N, et al. Enhancing tribological characteristics of titanium grade-5 alloy through hvof thermal-sprayed WC-Co nano coatings by topsis and golden jack optimization algorithm. Recent Patents on Nanotechnology,2025,19(4):544-567. DOI:10.2174/0118722105306841240808092616.

[9] Patel B. Novel Processing, Microstructure and Properties of a Cobalt-Chromium-Molybdenum Orthopaedic Alloy. London: University College London, 2012.

[10] Sohrabi S, Fu J, Li L, et al. Manufacturing of metallic glass components: Processes, structures and properties. Progress in Materials Science,2024,144:101283. DOI:10.1016/j.pmatsci.2024.101283.

[11] Haaja V,Varis T, Laurila J, et al. Fretting behavior of WC-Co-Cr coatings against QT steel in bolted joint. Journal of Thermal Spray Technology, 2024, 33(4): 1117-1134.DOI:10.1007/s11666-024-01732-4.

[12] Ma L, Eom K, Geringer J, et al. Literature review on fretting wear and contact mechanics of tribological coatings. Coatings, 2019, 9(8): 501. DOI: 10. 3390/COATINGS9080501.

[13] Li B, Li P, Zhou R, et al. Contact mechanics in tribological and contact damage-related problems: A review. Tribology International, 2022, 171:107534. DOI: 10.1016/j.triboint.2022.107534.

[14] Khonsari M M, Ghatrehsamani S, Akbarzadeh S. On the running-in nature of metallic tribo-components: A review. Wear, 2021, 474: 203871. DOI: 10. 1016/j. wear. 2021. 203871.

[15] Maxwell A S, Broughton W R, Dean G D, et al. Review of accelerated ageing methods and lifetime prediction techniques for polymeric materials. 2005: Report Number: Npl Report Depc Mpr 016. Https://api. semanticscholar. org/corpusid:182082742

[16] Maich A A,Gronsky R, Komvopoulos K. Microstructure evolution and fretting wear mechanisms of steels undergoing oscillatory sliding contact in dry atmosphere. Materials, 2024, 17(8): 1737. DOI: 10. 3390/ma17081737.

[17] Karbhari V M, Chin J, Hunston D, et al. Durability gap analysis for fiber-reinforced polymer composites in civil infrastructure. Journal of Composites for Construction, 2003,7(3):238-247. DOI:10.1061/(ASCE)1090-0268(2003)7:3(238).

[18] Wang G, Peng Y, Zhu Z, et al. A multi-physics coupling analysis to predict stress corrosion characteristics of wires in rope under wear damage. Simulation Modelling Practice and Theory, 2024, 131:102882. DOI:10.1016/j.simpat.2023.102882.

[19] Imran M, Wang D, Wang L, et al. Finite element modelling of effect of corrosion on fretting wear in steel wires. Tribology International, 2025, 206:110573. DOI: 10.1016/J.TRIBOINT.2025.110573.

[20] Elhadi A, Amroune S, Slamani M, et al. Evaluation of drilling by induced delamination of hybrid biocomposites reinforced with natural fibers: A statistical analysis by RSM. Journal of Composite Materials, 2024, 58(23): 2515-2530. DOI:10.1177/00219983241271035.

[21] Fnides M,Amroune S, Belaadi A, et al. Modeling and optimizing the alkaline treatment process to enhance the date palm fibers' tensile mechanical properties using RSM. Journal of Natural Fibers,2024,21(1): 2384663. DOI: 10.1080/15440478.2024.2384663.

[22] Kontou A, Taylor R I, Spikes H A. Effects of dispersant and zddp additives on fretting wear. Tribology Letters, 2021,69(1):6. DOI:10.1007/S11249-020-01379-6.

[23] Kolbas D, Pelcastre L, Prakash B, et al. Role of various influencing parameters on high temperature fretting behaviour of different tribopairs in liquid lead. Nuclear Materials And Energy,2024,40:101699. DOI:10.1016/j.nme.2024.101699.

[24] Dembiczak T, Kruzel R, NáPrstková N, et al. Abrasion wear analysis of commercial cutting inserts by ball-on-disc method. Manufacturing Technology, 2024, 24(5):738-746.

[25] NáPrstková N, Kruzel R, Dembiczak T. Tribological studies of monolithic drawing dies for the production of reinforcing wires used in construction. Budownictwo o Zoptymalizowanym Potencjale Energetycznym, 2022, 11: 23-30.DOI:10.17512/bozpe.2022.11.03.

[26] Zhu X. Tutorial on hertz contact stress. In Opti, 2012, 521:1-8.

[27] Shi Z, Xu L, Deng C, et al. Effects of frequency on the fretting wear behavior of aluminum bronze coatings. Surface and Coatings Technology, 2023, 457: 129306. DOI:10.1016/j.surfcoat.2023.129306.

[28] Fischer A, Nair S B, Herbig M, et al. Mechanisms of mechano-tribological imprinting in in vitro fretting corrosion of tialv/cocrmo couples. In Orthopaedic Proceedings, 2019, 101(supp_5): 21-21.

[29] Argatov I, Chai Y S. Contact geometry adaptation in fretting wear: A constructive review. Frontiers In Mechanical Engineering, 2020, 6: 51. DOI: 10.3389/fmech.2020.00051.

[30] Saada K, Amroune S, Belaadi A, et al. Enhancing the mechanical characteristics of eco-friendly composite materials: Taguchi and RSM optimization. Journal of Natural Fibers, 2024, 21(1): 2427704. DOI: 10.1080/15440478.2024.2427704.

[31] Saada K, Amroune S, Zaoui M. Prediction of mechanical behavior of epoxy polymer using artificial neural networks (ANN) and response surface methodology (RSM). Fracture and Structural Integrity, 2023, 17(66): 191-206. DOI: 10.3221/IGF-ESIS.66.12.

[32] Saada K, Zaoui M, Amroune S, et al. Exploring tensile properties of bio composites reinforced date palm fibers using experimental and modelling approaches. Materials Chemistry and Physics, 2024, 314: 128810. DOI: 10.1016/j.matchemphys.2023.128810.

[33] Saada K, Farsi C, Amroune S, et al. Examining the bending test properties of bio-composites strengthened with fibers through a combination of experimental and modeling approaches. Journal of Composite Materials, 2024, 58(12): 1483-1499. DOI: 10.1177/00219983241240819.

[34] Benyettou R, Amroune S, Slamani M, et al. Modelling and optimization of the absorption rate of date palm fiber reinforced composite using response surface methodology. Alexandria Engineering Journal, 2023, 79: 545 - 555. DOI: /10.1016/j.aej.2023.08.042.

[35] Saada K, Amroune S, Zaoui M, et al. Optimizing water Absorption's influence on composite mechanics through response surface methodology. Journal of Composite Materials, 2024, 58(21): 2327 - 2341. DOI: 10.1177/00219983241264357.

[36] Fnides M, Amroune S, Belaadi A, et al. Advanced optimization of alkalinization processes for date palm fibers using response surface methodology with Taguchi design (L16). Journal of Natural Fibers, 2025, 22(1): 2461492. DOI: 10.1080/15440478.2025.2461492.